Nanomechanical Model of Microtubule Translocation in the Presence of Electric Fields

Taesung Kim,* Ming-Tse Kao,† Ernest F. Hasselbrink,* and Edgar Meyhöfer*†
*Department of Mechanical Engineering and †Department of Biomedical Engineering, University of Michigan, Ann Arbor, Michigan 48109

ABSTRACT Research efforts in recent years have been directed toward actively controlling the direction of translocation of microtubules on a kinesin-coated glass surface with E-fields (electric fields), opening up the possibility of engineering controllable nanodevices that integrate microtubules and motor proteins into their function. Here, we present a detailed, biophysical model that quantitatively describes our observations on the steering of microtubules by electric fields. A sudden application of an electric field parallel to the surface and normal to the translocation direction of a microtubule bends the leading end toward the anode, because Coulombic (electrophoretic) forces are dominant on negatively charged microtubules. Modeling this bending as a cantilever deflection with uniform loading requires accurate mechanical and electrical properties of microtubules, including their charge density, viscous drag, and flexural rigidity. We determined the charge density of microtubules from measurements of the electrophoretic mobility in a "zero flow" capillary electrophoresis column and estimate it to be 256 e^- per micron of length. Viscous drag forces on deflecting microtubules in electroosmotic flows were studied theoretically and experimentally by directly characterizing flows using a caged dye imaging method. The flexural rigidity of microtubules was measured by applying E-fields to microtubules with biotinylated segments that were bound to streptavidin-coated surfaces. From the calculated loading, and the Bernoulli-Euler curvature and moment equation, we find that the flexural rigidity of microtubules depends on their length, suggesting microtubules are anisotropic. Finally, our model accurately predicts the biophysical properties and behavior of microtubules directed by E-fields, which opens new avenues for the design of biomolecular nanotransport systems.

INTRODUCTION

Nature has created a large variety of molecular motors, including kinesins, that play key roles in many cellular processes such as nano- and microscale transport and cell division. These motor proteins interact with cytoskeletal filaments (actin filaments or microtubules) to convert chemical energy (ATP) into mechanical force and motion, analogous to the way that electrical motors generate mechanical torque and rotational motion from electric energy. They are truly nanoscopic, can be readily expressed and purified as recombinant proteins and, under appropriate loading conditions, exhibit high efficiency (kinesins, for example, generate significant forces of ~6 pN with up to 50% chemomechanical energy conversion efficiency) (1,2). Thus, the use of biological motor molecules as transporters promises some distinct advantages over their man-made counterparts in nano- and microscale technological applications. Recently, kinesin motors and microtubules have been integrated as transport systems or actuators into first standalone and low power micro total analysis systems, and several other concepts of powering nanodevices and microfluidic devices have also been reported or proposed (3–5).

To date, one of the main technological challenges to developing useful molecular motor-powered devices is controlling the direction of movement along specific tracks to direct cargoes to precise targets. In the case of kinesin motors, the direction of translocation is determined by the orientation of the microtubule. In microtubule gliding assays, which are most frequently integrated into engineered device structures because of their robust motility, the direction of motion of microtubules is random. Hiratsuka et al. developed a passive method for controlling microtubule translocation by fabricating circular guide channels, which force the microtubules along a single path, coupled with arrowheads to rectify the translocation into a single direction around the circle (6). Subsequently, several other groups succeeded in guiding microtubules along a straight line using mechanical patterning or a combination of mechanical and chemical nanotracks (7,8), and others have demonstrated microtubule guiding using various nanopatterns (3,9–11).

Recently, attempts have been made to actively direct microtubules using flow fields (12–14) and electric fields (3,15,16) by imposing viscous drag or electrophoretic forces on moving microtubules. These external forces are believed to bend the leading end of microtubules into the direction of the applied forces; the remainder follows and eventually the entire microtubule is aligned with the direction of the applied force. Similarly, actin filaments have been aligned parallel to weak E-fields (electric fields) on a myosin-coated surface (17). Sträcke et al. studied the motility of microtubules under E-fields and characterized their electrophoretic mobility and charge density (15). Jia et al. attempted to use electrophoretic and dielectrophoretic forces to selectively sort microtubules approaching a bifurcation junction, but reported that dielectrophoretic forces are more effective than electrophoretic

Submitted May 14, 2007, and accepted for publication September 25, 2007.

Address reprint requests to Edgar Meyhöfer, University of Michigan Dept. of Mechanical Engineering, 2350 Hayward St., Ann Arbor, MI 48109. Tel.: 734-647-7856; Fax: 734-647-7856; E-mail:meyhofer@umich.edu.

Editor: David M. Warshaw.

0006-3495/08/05/3880/13 $2.00

doi: 10.1529/biophysj.107.112755

forces for steering microtubules (3). On the other hand, we recently demonstrated that steady E-fields, under appropriate conditions, can be used effectively to direct microtubules (18). Our work suggested that the kinesin surface density is a major factor in determining the alignment of microtubules with E-fields (18). We were able to demonstrate the guiding of microtubules along arbitrary paths (e.g., circles and figure-eights) by continuously manipulating the direction of the applied E-fields. Image sequences also showed the deflection of the leading end of microtubules toward the anode, further hinting at a microtubule cantilever mechanism based on Coulombic forces created by the E-field and the charge on the microtubule.

Attempts to quantitatively describe the E-field-based steering of microtubules using cantilever-beam theory have been frustrating, in large part due to disparities in the data required for such a model (3). The model requires knowing the charge density and flexural rigidity of microtubules, as well as the electroosmotic mobility (or ''zeta''-potential) of the glass substrate, and the drag coefficient(s) of the microtubule near the surface. Although the zeta-potential of glass in contact with aqueous electrolyte is quite well established (19), and drag coefficients are reasonably well approximated (20), the charge density and flexural rigidity measurements of microtubules (MT) show large variations in the literature. For example, Sträcke et al. estimate the linear charge density as $q'_{MT} = 280\ e^-/\mu m$ using electrophoresis data (15), whereas the electron crystallography data from Nogales et al. (21) suggest a charge density of $q'_{MT} = 14{,}400\ e^-/\mu m$ (>50 times higher). Minoura and Muto infer from dielectric measurements a net charge of 20 e^- per tubulin dimer, which corresponds to $q'_{MT} = 32{,}500\ e^-/\mu m$ (22). Also, the charge density depends on the pH, and the Coulombic force depends on the ionic strength of the buffer solution. Given the large differences in past measurements of the charge density and its dependence on the exact experimental conditions, our modeling work requires characterization of the electrophoretic properties of microtubules under appropriate buffer conditions.

The flexural rigidity of microtubules is the other key parameter in the model. Unfortunately, the flexural rigidity of microtubules seems to be affected by experimental methodologies (23) and the rate of polymerization (24). Experimental methods utilizing larger-scale mechanical perturbations with optical tweezers (25–27) or hydrodynamic flow (28) indicated that the flexural rigidity ranges from 1.9×10^{-24} Nm^2 to 4.9×10^{-24} Nm^2 (25–27) as deduced from the bending moment and the curvature. On the other hand, thermal fluctuation methods result in factor-of-five larger flexural rigidities, ranging from 22×10^{-24} Nm^2 to 26×10^{-24} Nm^2 (24,28–30) as inferred from the mode shapes of observed microtubule curvatures. It is noteworthy that the length of the microtubules used in methods applying (active laser trapping or hydrodynamic) mechanical perturbations was relatively shorter (2–23 μm) than that used in thermal methods (24–65 μm). Also, the effect of taxol (or paclitaxel), which is used in most experiments to stabilize microtubules against depolymerization, on the flexural rigidity needs to be considered. In addition, it has recently been suggested that the flexural rigidity is dependent on the microtubule length, hinting at an unexpected anisotropy of microtubules (31–37). Given all these uncertainties, it is imperative to characterize the biophysical properties of the microtubules as used in our experiments. To this end we report what we believe is a new method for measuring the flexural rigidity of microtubules using E-fields.

In this article, we combine a nonlinear, analytical solution of an elastic cantilever beam with our measured biophysical properties of microtubules. The resulting model provides an accurate nanomechanical model of the deflection and translocation behavior of kinesin-powered microtubules in the presence of E-fields. The agreement between our model predictions and experiments also lends additional, strong support to the observed fundamental mechanical and electrical properties of microtubules, including their length-dependent flexural rigidity.

EXPERIMENTAL METHODS AND MATERIALS

Kinesin and microtubule purification

For most experiments, we used a bacterially expressed kinesin motor, NKHK560cys. This motor consists of the head and neck domain of *Neurospara crassa* kinesin (amino acids 1–433) and stalk of *Homo sapiens* kinesin (residues 430–560) and a reactive cysteine at the C-terminal end (38). Kinesin was expressed and purified as described previously (11,38). Tubulin was purified from cow brain by three cycles of microtubule polymerization and depolymerization followed by phosphocellulose ion exchange chromatography, and fluorescently labeled tubulin (TMR-tubilin) was prepared by reacting polymerized microtubules with a 20-fold excess of tetramethylrhodamine (Invitrogen, Carlsbad, CA) at room temperature for 30 min. Competent, labeled tubulin was purified from this mixture by repeated depolymerization and polymerization. For all experiments, microtubules were polymerized by incubating 2 mg/ml tubulin (equal ratios of TMR-labeled and unlabeled tubulin), 1 mM GTP and 4 mM $MgCl_2$ in BRB80 buffer at 37°C for 20 min. Microtubules were stabilized by the addition of 10 μM taxol. All motility assays were carried out in BRB80 buffer at pH 6.8 at room temperature. For motility assays, we incubated our microchannel motility chambers with 100 μL of a 0.694 μM kinesin solution in casein-BRB80 for 5 min as previously described (20). Although this treatment leads to ~10 times lower kinesin surface densities compared to the largest concentrations (~10 μM) of kinesin we have tested, the resulting motility remains a high density assay in which microtubules glide uninterrupted over large distances. We used these reduced kinesin surface-density conditions to facilitate the analysis of the electric field-induced steering of microtubules (see below).

Construction of microchannels for gliding assays

Microchannels were constructed using conventional 75 μm thick double-sided tape (Tesa 5338, Beiersdorf, Hamburg, Germany) as a spacer. On a bare cover glass (22 × 54 × 0.17 mm), four pieces of tape were attached on the edges to make two 4 mm wide channels that intersected together, and then a slender grease seal was applied at the interior edge of the tape to prevent contamination of the solution from constituents of the tape's glue. Subsequently, another cover glass (15 × 15 mm) was carefully placed on top of the double-sided tape to complete the channel structures. Glass pipette reservoirs

that act as ports to the microchannels were bonded with epoxy on top of the gaps between bottom and top cover glasses, and the open sides were sealed. Fig. 1 shows the schematic view of the microchannel system. Four individually controllable platinum electrodes were inserted into the reservoirs that were connected to relay circuits, which can be operated with a personal computer via DAQ board and LabVIEW (National Instruments, Austin, TX). With this experimental setup, we can create E-fields of various magnitude and directions on microtubules translocating around the intersection region.

Measurement of the electrophoretic mobility of microtubules

The electrophoretic mobility of microtubules was measured with a ''zero-flow'' capillary (CE-100SA, MicroSolv Technology, Eatontown, NJ), which does not generate electroosmotic flow (EOF) because a proprietary coating (polyacrylamide or methylcellulose) suppresses the zeta-potential of the interior glass surface. A fluorescent microscope (Olympus IX71, Center Valley, PA) equipped with photomultiplier tube (PMT H8568-02, Hamamatsu, Hamamatsu City, Japan) was used to detect the signals that come from a small optical window in the fiber (Fig. 2). The window was made by burning off the protective polyimide coating of the fiber in a narrow region. The capillary was rinsed with 10 mM NaOH for 10 min and then rinsed with deionized water for 10 min before loading it with buffer solution (80 mM PIPES adjusted to pH = 6.8 with potassium hydroxide). A narrow plug of microtubules was inserted into the fiber by dipping one end of the capillary into the labeled microtubules solution (0.03 mg/ml) and then applying high voltage for several seconds. The capillary end was then moved back into the buffer reservoir, the power supply (E3612A, Agilent Technologies, Santa Clara, CA) was turned on and the signal from the PMT was acquired via a data acquisition system to precisely record the time when the microtubule plug passed the detection window. From the measured time and the run length of the capillary, the electrophoretic mobility of microtubules was obtained.

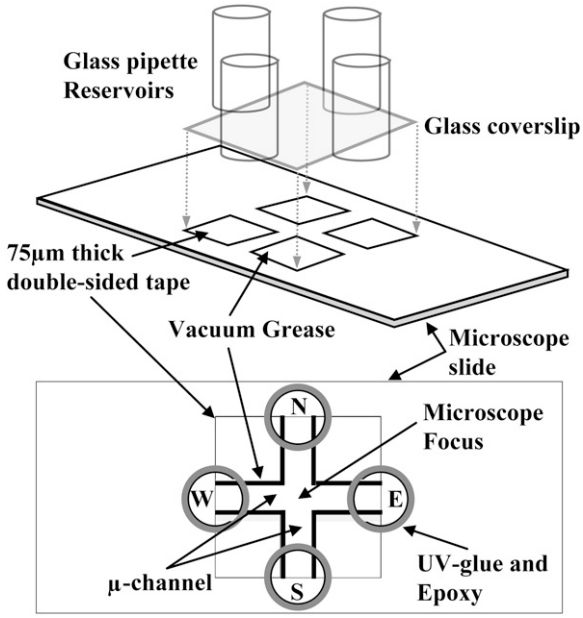

FIGURE 1 Microchannel fabrication. A microscope slide was used as substrate and then four 75 μm thick double-sided tapes were attached symmetrically, 4 mm apart. A slender grease seal was applied at the interior edge of the tape to prevent contamination of the solution from constituents of the tape's glue. Subsequently, a cover glass was put on top of the double-sided tape and the glass pipette reservoirs were bonded with ultraviolet epoxy. N, E, S, and W denote the north, east, south, and west electrode, respectively.

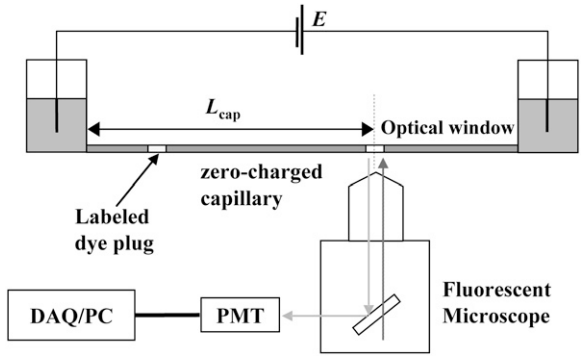

FIGURE 2 Electrophoresis experiment setup. The electrophoretic mobility of microtubules was determined by recording the migration velocity in a zero-flow capillary using a fluorescence microscopy and a sensitive PMT.

Measurement of the electroosmotic mobility (zeta-potential)

Electroosmotic mobility of the standard buffer solutions (without the ''zero flow'' coating, but with casein/kinesin adsorbed to the glass surface) is measured via caged-dye velocimetry (39). The capillary was filled with a solution of caged dye (5-(and-6)-carboxy-Q-rhodamine, CMNCBZ-caged, Invitrogen) in the 80 mM PIPES buffer solution (the same used in gliding assays). The beam of a pulsed frequency-tripled Nd:YAG laser (λ = 355nm; pulse width 4 ns, 2 mJ/pulse) (Minilite, Continuum, Santa Clara, CA) was focused into the capillary to cleave the caged, fluorescent dye locally, creating a band of fluorescent species in the microchannel. The velocity of the flow is inferred from the subsequent advection of the dye in the channel. The uncaged dye band at two different times is shown in Fig. 3, *a–b*; a plot of the fluorescence intensity is shown in Fig. 3 *c*. Due to diffusion, the distribution of the band widens with time, but the movement of the peaks of the two bands gives the displacement, which is divided by the elapsed time to obtain the ''apparent'' velocity. However, this apparent velocity includes components due to electroosmosis of the bulk fluid, plus electrophoretic drift of the dye. The electroosmotic mobility is obtained by subtracting the electrophoretic mobility of the uncaged dye (40).

The dye's electrophoretic mobility was measured by again using a ''zero flow'' capillary in the same setup as shown in Fig. 2. For these measurements the caged dye was completely uncaged before the experiment via exposure to a ultraviolet lamp (UVGL-25, UVP, CA) for ~10 h.

Measurement of flexural rigidity of microtubules

To measure the flexural rigidity of individual microtubules, we polymerized fluorescently labeled microtubules with short, biotinylated center portions (weakly fluorescently labeled) and long plus-ends. These microtubules were bound with their biotinylated center portion via streptavidin to a surface coated with biotinylated bovine serum albumin (BSA). The following experimental protocol was used: first, 2 μL of 10 mg/ml biotinylated BSA was diluted with 98 μL of the buffer solution and loaded into the microchannel assay system, and incubated for 3 min. Second, 10 μL of 1 mg/ml streptavidin mixed with 90 μL of the buffer solution was loaded and incubated for 3 min. Finally, after the remaining streptavidin was removed with 100 μL of buffer solution, the segmented microtubules were loaded into the microchannel using exactly the same condition used for gliding assays, except no kinesin was present. We then recorded the bending curvatures of microtubules in the presence of E-fields, as seen in Fig. 4 *a*, by using an inverted epifluorescence microscope (Axiovert 200, Carl Zeiss Microimaging, New York) equipped with a digital charge-coupled device camera (Orca ER II, Hamamatsu). Since the plus-ends of the microtubules did not bind to the surface, their deflections toward the anode in response to different E-fields

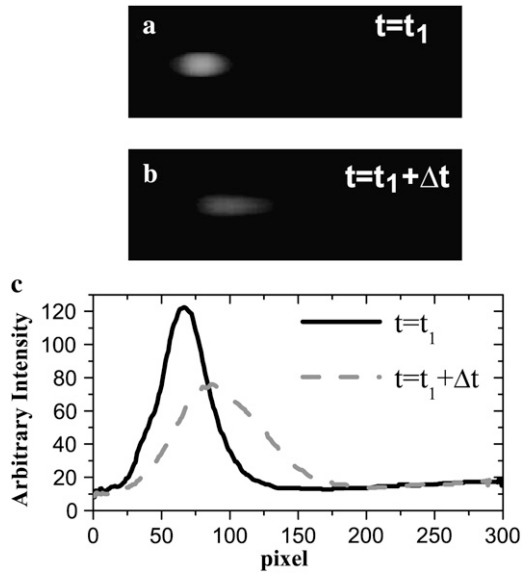

FIGURE 3 Electroosmotic mobility. Observed images from a charge-coupled device camera of uncaged dye as a function of time. (*a*) Caged dye is uncaged by exposing it to laser light ($\lambda = 350$ nm). (*b*) The image was acquired several seconds after an E-field is applied. A wide distribution of uncaged dye is due to axial diffusion. Electroosmotic mobility can be derived from the displacement of the two bands and the elapsed time. (*c*) Plots showing the intensity profiles of the fluorescent dye bands along the microchannels at two different times.

could be readily observed. In Fig. 4 *b*, ensemble-averaged image of a microtubule in the absence of an E-field is superposed on another ensemble-averaged image of the microtubules in the presence of an E-field. Images such as these were obtained from 50–100 ensemble images, corresponding to 10–20 s observation to average out the effects of thermal fluctuation. As the flexural rigidity is believed to be affected by physiological buffer solutions, taxol, and temperature (30,32), all measurement were conducted at the same temperature and with the same buffer solutions used for all gliding assays.

The microtubule shape was determined by using a custom MATLAB (The MathWorks, Natick, MA) image processing script that seeks, along a vertical row of pixels near the free end of the microtubule, three consecutive high-intensity pixels to approximately locate the microtubule. A polynomial fit to the intensity values was used to find the center of the microtubule to within subpixel accuracy ($\sim\pm 0.15$ μm). This process was repeated for the next column by moving toward the ''clamped'' end of the microtubule. An example of the data obtained is shown in Fig. 4 *c*, which shows results for cases with and without applied E-fields. From this data, the location of the clamped portion of the microtubule can be determined because the curves merge. The points were independently verified by image processing, exploiting the fact that the biotinylated (''clamped'') part was labeled differently from the free segment.

Even in the absence of E-fields, a small but nonzero curvature may exist due to some stresses imposed by the binding of the biotinylated portion to the surface as well as the intrinsic curvature of the microtubule. By subtracting the initial curve $y_0(x_0)$ from the curvature in the presence of E-field $y_1(x_1)$, the deflection produced by the applied E-fields $\nu(x)$ was obtained as $\nu(x) = y_1(x_1) - y_0(x_0)$. We note that x_0 and x_1 satisfy $\int_0^{x_0}\sqrt{1+(y_0')^2}dx = \int_0^{x_1}\sqrt{1+(y_1')^2}dx$ because the total microtubule length is constant ($\lambda_{MT} = \int_0^{x_L}\sqrt{1+(dy/dx)^2}dx$, where x_L is the end point of the initial curvature). Fig. 4 *c* shows the digitized curves and least-square-error curve fit using a second-order polynomial, which produced the length of microtubules, the maximum deflections, the initial bias angles between the perpendicular direction of

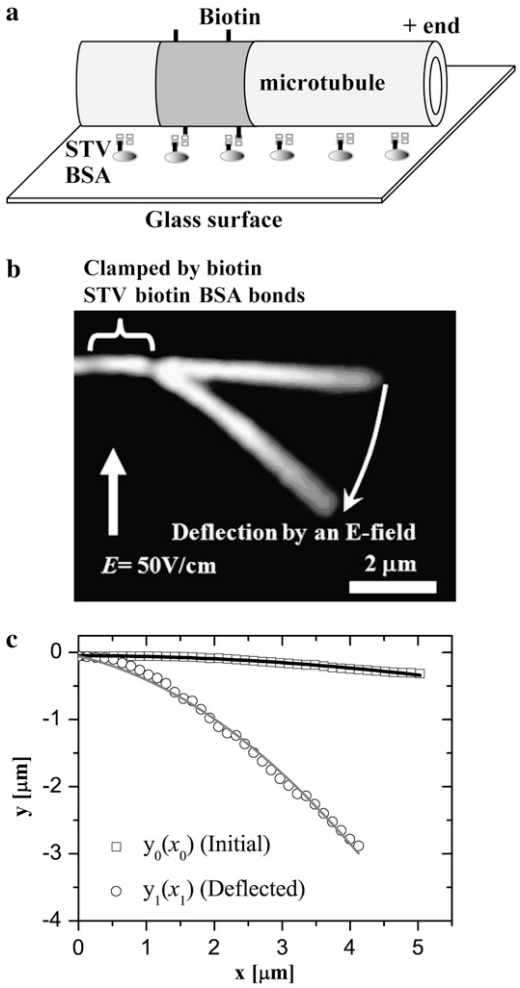

FIGURE 4 Flexural rigidity of microtubules. (*a*) A partly biotinylated microtubule is attached to a BSA-coated surface via streptavidin linkages. The biotinylated segment is lightly labeled with rhodamine dye, whereas the remainder of the microtubule has no biotin binding sites and is more strongly fluorescently labeled (52). (*b*) Ensemble averaged images of the microtubules in the absence of the E-field and in the presence of an E-field (50 V/cm). When an E-field is applied, the biotinylated part of the microtubule that appears dimmer stays clamped, whereas the remaining, bright portion deflects toward the anode. Both images were obtained by averaging 50–100 frames, corresponding to 10–20 s of observation, to eliminate thermal fluctuations. (*c*) The squares denote the initial curvature of the microtubule in the absence of the E-field, whereas the circles denote the curvature of the microtubule in the presence of the E-field.

E-fields, and the initial direction of microtubules. In addition to these geometrical parameters, the applied bending moment is also necessary so that the flexural rigidity is calculated. The bending moment generated by the electrophoretic force and the viscous drag force by EOF are formulated below.

RESULTS

Active directional control of microtubules with E-fields

By way of example, Fig. 5 shows typical results from applying E-fields to translocating microtubules. Normally, mi-

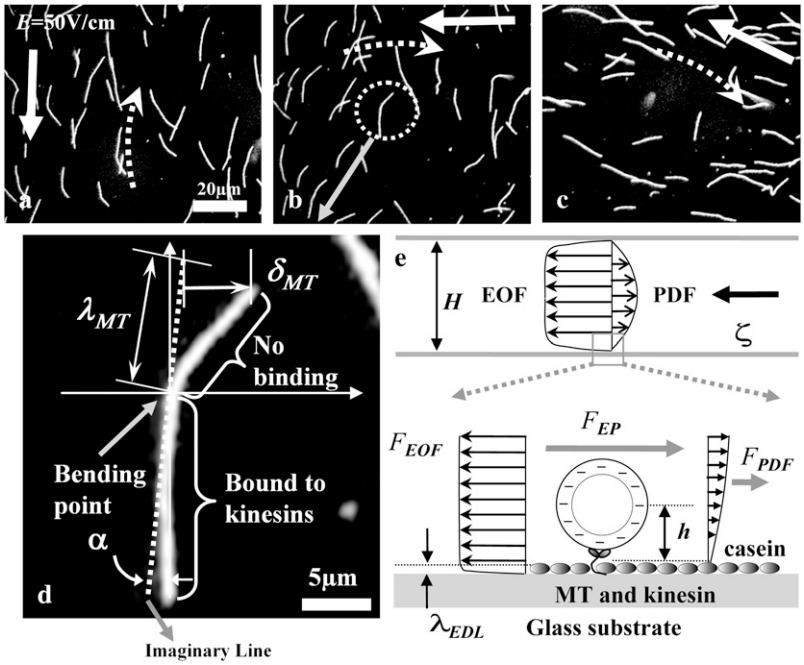

FIGURE 5 Directional control of microtubules. Transient bending behavior of microtubules controlled to translocate along an arbitrary dotted-line circle after a 90° direction change of a 50 V/cm E-field. In *a*, the applied E-field points in a downward direction, guiding microtubules to translocate upward. (*b*) When the E-field vector (*large arrow*) is suddenly changed to the left, the leading ends of microtubules bend immediately rightward. (*c*) After a short time, the remainder of each microtubule becomes aligned as well (the direction of the E-field is slightly biased by 26° for next direction control). (*d*) An example of a transiently cantilevered microtubule. Estimates of the length (λ_{MT}), the bias angle (α), and the maximum deflection (δ_{MT}) were obtained via image processing. (*e*) The electrophoretic force (F_{EP}), the viscous drag caused by EOF (F_{EOF}), and the viscous drag caused by PDF (F_{PDF}) are uniformly imposed on the microtubule and parallel to the E-field. The size of the MT and kinesin are not drawn to scale. The distance from the surface to the axis of the microtubule, h, is ~21.5 nm (20) and the λ_{EDL} is <1 nm (41). The height of the microchannel, H, is ~75 μm and ζ denotes the zeta-potential of glass surfaces ($\zeta = -18.7$ mV). The casein layer is ~8 nm in thickness (53).

crotubules in a gliding assay move in an even (random) distribution of directions. However, as shown in Fig. 5 *a*, when an E-field is applied in one direction (downward), the leading ends of the microtubules redirect in the opposite direction (upward), because the dominant electrophoretic force draws the negatively charged microtubules. The image shown in Fig. 5 *a* is taken several seconds after the application of the E-field. The dynamics of the response to a sudden change in an E-field is shown in Fig. 5 *b*. Here the E-field direction changes from downward to leftward, and the microtubules redirect their directions again toward the anode as seen in Fig. 5 *b*; the situation ~20 s later is shown in Fig. 5 *c*, showing that most of the microtubules are highly aligned, with the translocation direction opposite to the E-field. In Fig. 5 *c*, the direction of the E-field is slightly biased by 26° upward to control the microtubules to translocate along an arbitrary direction indicated with dotted-line arrows. Using this approach, we can actively guide microtubules along any desired trajectory, without any mechanical or chemical patterns.

The above experiments allowed us to make the following key observations (18): Upon application of the E-field, the leading end of a microtubule appears sharply bent, but the remainder of the microtubule remains on its former trajectory. This suggests that the sharply bent portion at the leading end of the microtubule is not bound to kinesin, but the rest of the microtubule remains bound. The rate of alignment of translocating microtubules in an E-field depends on the strength of applied E-fields, the surface density of kinesin, and the translocation velocity of microtubules. A relatively low surface density of kinesin results in faster alignment; typically, 50 V/cm results in >90% of the microtubules being aligned to within some small tolerance in ~30 s at lower concentrations of kinesin. Furthermore, chemical treatment of the glass surface does significantly change the absorption of kinesin. For instance, subjecting a cover glass to Piranha clean (H_2O_2:H_2SO_4 = 1:1) for 10 min, followed by etching with 2.5% hydrofluoric acid for 10 s, and deionized water rinse for 10 min appears to increase the surface density of kinesin noticeably because the density of microtubules in standard gliding assays on chemically treated cover glasses at a low concentration of kinesin (10–40 times lower) is comparable to that on untreated cover glasses at a normal kinesin concentrations (8). We have reported a detailed statistical analysis of the E-field response of microtubules in gliding assays to further support these observations (18).

The above observations form the basis of our cantilever model. We introduce the model by beginning from our image processing analysis. First, as seen in Fig. 5 *d*, we set the origin of a coordinate system at the bending point, and choose the x axis as parallel to the E-field. Every bending point is carefully determined as that point where deflections appear to begin (similar to the clamped wall boundary of a cantilever beam; see Appendix A). Second, we introduce an imaginary line (*dotted line* in Fig. 5 *d*) that is tangential to the clamped segment of the microtubule at the bending point and assumed that this line is the original trajectory of the microtubule (the original curvature of the cantilevered portion). We use this tangent to define (and measure) the deflection (δ_{MT}), the length of leading end (λ_{MT}), and the incident angle α (the angle between the imaginary line and the y axis). Third, if λ_{MT} is gradually increasing from frame to frame, but δ_{MT} is not getting larger, the cantilevered portion of λ_{MT} is unlikely to reach equilibrium because additional interactions between kinesin(s) and the microtubule limit further deflection. In this

case, we discard the data sample. Finally, we linearly compensate for the deflection data by dividing δ_{MT} by $\cos(\alpha)$ as follows (see Appendix A):

$$\delta_{obs} = \frac{\delta_{MT}}{\cos(\alpha)}. \quad (1)$$

The above equation allows us to exclude the effect of the incident angle on the deflection of individual microtubules, making it possible to compare the model's result with the observed deflections. Following the above image analysis and data processing, the observed microtubule deflections in gliding assays as a function of cantilever lengths are plotted for E-fields of 20 V/cm and 50 V/cm (see Fig. 7).

Cantilever model: bending moment and deflection

The deflection of a cantilever beam is a function of the bending moment and the flexural rigidity. As seen in Fig. 5, *d–e*, the bending moment imposed on the microtubule by an E-field consists of $\boldsymbol{F}_{EP}$ on the negatively charged microtubule, $\boldsymbol{F}_{EOF}$ is caused by the electroosmotic flow on glass substrates, and $\boldsymbol{F}_{PDF}$ is created by pressure-driven flow (PDF) due to any hydrostatic pressure difference between the buffer solution reservoirs. All these forces are parallel to the E-field, and all of them create uniform loading on the microtubule. Note that $\boldsymbol{F}_{EOF}$ is directed opposite to $\boldsymbol{F}_{EP}$ and $\boldsymbol{F}_{PDF}$, because the surface or ''zeta'' potential, ζ, of glass surfaces has a negative value. We therefore write the uniform load (N/m) caused by an E-field as follows:

$$\boldsymbol{\omega}_{MT} = (\boldsymbol{F}_{EP} + \boldsymbol{F}_{PDF} + \boldsymbol{F}_{EOF})/\lambda_{MT}. \quad (2)$$

As mentioned before, the effect of $\boldsymbol{F}_{PDF}$ in our experiments is negligible, because any head height due to EOF can only be accumulated very slowly as our reservoirs have large diameters (6 mm). Furthermore, since the height of the microtubule from the surfaces is an order of magnitude less than that of the microchannel depth ($h \ll H$), the shear stress by any PDF is small enough to be neglected. Therefore, the electrophoretic force and the viscous drag force are dominant.

$\boldsymbol{F}_{EP}/\lambda_{MT}$ is the electrophoretic force per unit length. Since microtubules consist of α- and β-tubulin subunits that are negatively charged, the force is assumed to be very uniform along the axis of microtubules. The electrophoretic force is then calculated as follows:

$$\boldsymbol{F}_{EP}/\lambda_{MT} = q'_{MT}\boldsymbol{E}. \quad (3)$$

Here, q'_{MT} is the charge density per unit length of microtubules, and $\boldsymbol{E}$ is the strength of the applied E-field. $\boldsymbol{F}_{EOF}/\lambda_{MT}$ corresponds to the viscous drag force caused by electroosmotic flow. In very low Reynolds number flows, the drag force is calculated as

$$\boldsymbol{F}_{EOF}/\lambda_{MT} = C_i \eta \boldsymbol{u}_{EOF}, \quad (4)$$

where C_i is the drag coefficient of a long and slender cylinder in fluids, i denotes the orientation of the cylinder, η is the dynamic viscosity of the buffer solution (at 24°C, $\eta = 0.91 \times 10^{-3}$ Pa·s), and $\boldsymbol{u}_{EOF}$ is the electroosmotic velocity (i.e., EOF velocity is $\boldsymbol{u}_{EOF} = \mu_{EOF}\boldsymbol{E}$, where μ_{EOF} is the electroosmotic mobility) (41).

In general, $\boldsymbol{F}_{EOF}$ depends on the electric double layer (EDL) thickness, λ_{EDL}, because the $\boldsymbol{u}_{EOF}$ varies within the λ_{EDL} along the vertical axis. That is, if the microtubules were translocating within the EDL, the drag would be a very complicated function of h, λ_{EDL}, and other parameters. Fortunately, under all experimental conditions in this study, λ_{EDL} is <1 nm ($\lambda_{EDL} \approx 9.61\text{nm}/\sqrt{\sum_i z_i^2 c_i}$, where z_i and c_i are the valence and the concentration of species in buffer solutions, respectively, (41)), and the distance h from the top surface of casein adsorbed on glass surfaces to the center line of microtubules is ~21.5 nm (20). We assumed that the no-slip boundary condition is satisfied on the top surface of a casein layer instead of the glass substrate. Thus, all microtubules likely translocate well outside of the EDL ''boundary layer'', and therefore the EOF approaching the microtubule is very nearly uniform. Hunt et al. (20) reported theoretical drag coefficients of $C_\perp = 4\pi/[\ln(\lambda_{MT}/2r_0) + 0.84]$ (perpendicular to the cylinder) and $C_\parallel = 2\pi/[\ln(\lambda_{MT}/2r_0) - 0.2]$ (parallel to the cylinder), where $2r_0$ is the diameter of the cylinder. In this study, we take $2r_0 = 30$ nm. Therefore, Eq. 4 becomes

$$\boldsymbol{F}_{EOF}/\lambda_{MT} = C_\perp \eta \mu_{EOF}\boldsymbol{E} \quad (5)$$

in case of the perpendicular microtubules to E-fields. In addition, since λ_{EDL} is much less than the depth of the channel (1 nm vs. 75 μm), the μ_{EOF} is also given as follows:

$$\mu_{EOF} = -\varepsilon\zeta/\eta. \quad (6)$$

Here, ε is the permittivity ($\varepsilon = 80 \times 8.854 \times 10^{-12}$ C^2/Nm^2) and ζ is the zeta-potential of glass substrate at the gliding assay buffer solution.

We now turn to the mechanics model for the cantilever bending. From the Bernoulli-Euler curvature and moment equation and our derivation from Eq. 2 through Eq. 6, we complete the linear cantilever model for microtubule deflection as follows (see Appendix A, Eq. A3):

$$\delta_{model}(\lambda_{MT}) = \frac{(q'_{MT} + C_\perp \eta \mu_{EOF})E}{8EI_{MT}} \lambda_{MT}^4. \quad (7)$$

We first adopted the most favorable literature values for our model inputs to validate the model against observed deflections. Nonetheless, we found that this model failed to describe the observed deflections. We then noted that this solution is the linearized solution that neglects the nonlinearity in the beam equation. However, even if we included the nonlinear terms (exact analytical solution), we could not resolve the disparity between our data and model predictions. Given some substantial variation in the literature values for

important model inputs, we believed that it was imperative to confirm the literature values for charge density of microtubules, electroosmotic mobility of buffer solutions on glass surfaces, and the flexural rigidity of our microtubules.

Charge density of microtubules (q'_{MT})

As reported in Fig. 2, we observed an electrophoretic mobility of microtubules as measured by $\mu_{MT} = -L_{cap}/\Delta t/E = -(3.0 \pm 0.2) \times 10^{-4}$cm^2/Vs (mean $\pm$ SD, $N = 18$), where the average elapsed time (Δt) was 18.52 min. The electrophoretic mobility measured in our experiment was ~15% larger than that measured by Sträcke et al. (15). There might be several reasons for this, but the average length of microtubules probably generates the largest error because longer microtubules have less drag forces per unit length than shorter microtubules due to length-dependent drag coefficients (as can be readily seen from the equations discussed above). In addition, lower ionic strength leads to reduced electrophoretic mobilities and, since the dye used to label the microtubules is also negatively charged, it could affect the mobility of the microtubule. On the other hand, this effect is negligibly small because the number of charges per unit length due to tubulin is much greater than that due to dye molecules. The electrophoretic force is $F_{EP} = q'_{MT}EL_{MT}$, where q'_{MT} is the charge density of a microtubule per unit length and L_{MT} is the average length of the microtubule (measured as 11 μm). The viscous drag force is calculated as $F_{drag} = C_{eff}\eta\mu_{MT}EL_{MT}$, where C_{eff} is the effective drag coefficients of microtubules and assumed to be $C_{eff} = (C_{\parallel} + 2C_{\perp})/3$ (15). The charge density of microtubules was calculated as

$$q'_{MT} = C_{eff}\eta\mu_{MT}. \quad (8)$$

Using our measurements and the parameters discussed above, the charge density was inferred as $q'_{MT} = 256\ e^-/\mu$m, which is ~10% less than that reported by Sträcke and co-workers (15).

Electroosmotic mobility (μ_{EOF})

F_{EOF} is proportional to μ_{EOF} of buffer solutions on glass substrates, which varies significantly with the pH and the ionic strength of buffer solutions. From the intensity profiles of the fluorescent dye bands in Fig. 3, the apparent velocity was measured and then decomposed into

$$\boldsymbol{u}_{app} = \boldsymbol{u}_{EOF} + \boldsymbol{u}_{EP}. \quad (9)$$

The measured mobility was $\mu_{app} = (0.35 \pm 0.03) \times 10^{-4}$ cm^2/Vs (mean $\pm$ SD, $N = 12$). The electrophoretic mobility of the uncaged dye was also measured as $\mu_{EP} = -(1.14 \pm 0.18) \times 10^{-4}$ cm^2/Vs (mean $\pm$ SD, $N = 13$). Since $\mu_{app} = \mu_{EOF} + \mu_{EP}$, the average electroosmotic mobility was found as $\mu_{EOF} = (1.49 \pm 0.21) \times 10^{-4}$ cm^2/Vs. From μ_{EOF}, the zeta-potential of glass substrate was computed as $\zeta = -18.7$ mV (see Eq. 6) for our experimental conditions. The electroosmotic mobility is known to be affected by Joule heating when the permittivity and the viscosity of the buffer solution changes (42). In our experiments the temperature increase of the buffer solution for the maximum field strength of 50 V/cm was <3°C within 1 min. Therefore, the effect of Joule heating was neglected.

Flexural rigidity of microtubules (EI_{MT})

The flexural rigidity of microtubules was calculated from the deflection data of the immobilized microtubules (Fig. 4 *c*) and the exact analytical solution of the cantilever beam deflection (Eq. A14). We note that the linear solution (Eq. A3) for a cantilever beam, which has been used in most previous studies, has a significant error in the case of large deflections compared to the exact nonlinear solution (Eq. A14). The flexural rigidity values were measured by applying different strength of E-fields ranging from 5 V/cm to 50 V/cm at 5 V/cm intervals (Fig. 6). To eliminate the nonlinearity that may arise with large deflections (strong E-fields), such as cross-section deformation and local buckling (see Appendix B), the rigidity values from small deflections (when the deflection is <20% of the cantilever length) are compared to the averaged values, resulting in good agreement.

An important observation from our measurements is the dependence of the flexural rigidity on microtubule length. We observed an order of magnitude difference in the flexural rigidity between short microtubules and long microtubules. This length-dependent flexural rigidity is consistent with the results by Kurachi et al., who buckled microtubules with optical trapping forces (31) and by Takasone et al., who bent and compressed microtubules in the same manner (33). In addition, Pampaloni et al. reported that thermal fluctuations of short and long microtubules lead to an order of magnitude difference in a persistent length, which is also consistent with

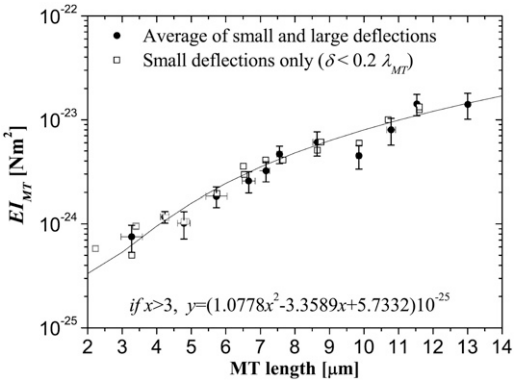

FIGURE 6 Flexural rigidity versus cantilevered microtubule length. The dependency of the flexural rigidity on the length was attributable to the anisotropic structure of microtubules and the curve-fit is based on the second order of the length ($EI_{MT} \sim \lambda^2_{MT}$) (31,33).

our results (37). This dependence of the flexural rigidity on length may be attributed to the anisotropic structure of microtubules and is crucial in resolving the disparity between our experimental observations and the cantilever model we reported above (in Eq. 7).

Comparison of the model and experimental observations

When we use all our measured values, including the mechanical and electrical properties of microtubules, for the presented linear cantilever model (Eq. 7), the model successfully accounts for the observed deflections of cantilevered microtubules under a light load, e.g., an E-field of 20 V/cm, as shown in Fig. 7 *a*. In this case, our linear cantilever model predicts the deflections well for the entire range of the cantilevered length because the linear solution has a negligible error in case of small deflections. However, under a heavy load (e.g., 50 V/cm) and larger microtubule deflections, the linear model fails to explain the experimental data; we suspected this because this solution neglects the geometrical nonlinearity.

The exact nonlinear solution for the bending of an elastic cantilever beam subject to a uniformly distributed load (or under self-weight) is given in Appendix A (see also Frisch-Fray (43)); this model accounts for large deflections, but assumes that the beam cross section is unchanged. This nonlinear elastic model can reasonably predict the experimentally observed deflections in both 20 V/cm (relatively small deflections) and 50 V/cm (relatively large deflections), respectively, as seen in Fig. 7. The predicted values given by our model are slightly less than the experimental observations. This may be because the cross section of the microtubule slightly changes under a large bending moment. In particular, the differences seem to be larger at a heavy load and at a long range of the cantilevered length in which the moment of inertia of the microtubule cross section may easily decrease, exhibiting even larger deflections. A more detailed discussion of an ovalization model of the microtubule cross section is presented in Appendix B.

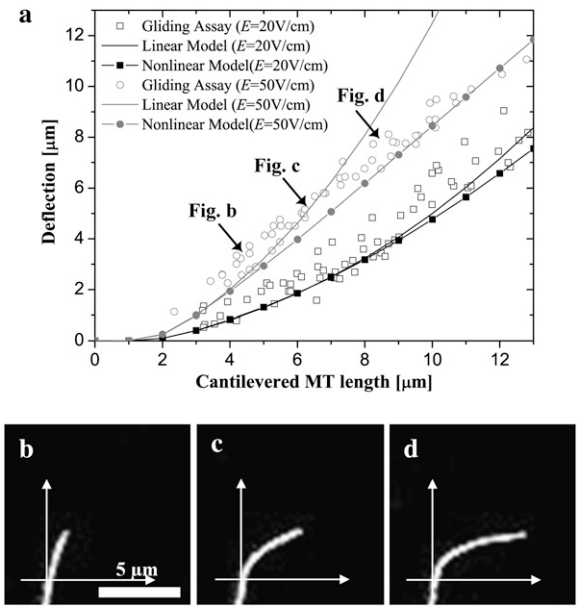

FIGURE 7 Comparison of model and experimental microtubule deflections. In *a*, the maximum deflections of microtubules are shown under 20 V/cm and 50 V/cm E-fields. The squares denote experimentally observed deflections under 20 V/cm. The dash-dot line with squares represents the nonlinear model and the dash-dot line represents the linear model. The circles denote the experimental deflections under 50 V/cm. The dash line and the dash line with circles represent the simple linear model and the nonlinear model, respectively. In *b–d*, a microtubule loaded in an E-field of 50 V/cm gradually deflects as it translocates and its cantilevered length increases with time.

DISCUSSION

By manipulating the vector direction of E-fields, we successfully confirm our own work (18) and that of others (3,15,16) that moving microtubules in kinesin-based gliding assays can be controlled to translocate in desired directions. Usually, a 50 V/cm E-field requires ~30 s to change the direction of most microtubules by 90°. Fortunately, gliding assays for micro- and nanotechnology applications move for tens of minutes to many hours, depending on the exact experimental conditions, allowing ample time for the control of microtubules. Also, the resulting turning radii (10–20 μm) of steered microtubules are consistent with the envisioned technical applications. E-fields have been thought to have some drawbacks, such as hydrolysis and Joule heating of the buffer solutions, which may deteriorate the motility. Nevertheless, E-fields have proved to represent a powerful active control method because the wide ranges of strength and various directions of E-fields are easily adjustable.

The image processing for measuring the deflection and the cantilevered length of microtubules has the largest uncertainties in the experimentally observed data (refer to Fig. 5 *d*). In contrast to the uncertainty in measuring the deflection of immobilized microtubules, the data analysis of microtubules in gliding assays poses two additional challenges: first, they are continuously moving at a speed of ~1 μm/s, so that the length of the cantilevered portion continuously changes. This hinders ensemble-averaging of both the deflection and the length. The second difficulty is that the initial curvatures of moving microtubules (before the direction change due the action of the applied E-field) are indeterminate, and only the deflected curvatures are measurable for a short time. In this work, by ''clamping'' a portion of the microtubules, the deflections were measured from an extrapolated trajectory (imaginary line (*dotted line* in Fig. 5 *d*)). However, it is worth noting that the longer the cantilevered microtubules are, the less they tend to be straight, because the effects of thermal fluctuation and internal stress on the microtubules are predominant. This will increase the discrepancy between the experimental observations and the model.

Another uncertainty may come from the cantilevered length that was measured from the negative end to the (assumed) last kinesin binding point. If a bending point's location is determined accurately and active kinesins clamp tightly the remainder of a microtubule, two ideal boundary conditions can be satisfied at that point without error (see Appendix A). But, in reality, the location of bending points can only be estimated and it is also not apparent whether kinesin binding to the microtubule acts as an ideal, fixed boundary condition. Nevertheless, bending points were estimated first by a careful analysis of consecutive image sequences that showed gradual deflections of microtubules with time. Subsequently, if these points seemed to satisfy the ideal boundary conditions, as the microtubules advanced and underwent distinct deflections, they were regarded as appropriate bending points. The above procedure was repeated so that the error did not represent more than two pixels ($\sim\pm$ 0.65 μm).

The nonlinear cantilever model is based on several mechanical and electrical properties of microtubules, which also have associated uncertainties. First, the charge density of microtubules was calculated by assuming that the orientations of microtubules continued to change during the electrophoretic mobility measurement. This assumption led to adopting an effective drag coefficient, but it does not attempt to account for tumbling microtubules. In general, however, this effect is more important in high Reynolds number flows than in creeping flows such as encountered here. For example, if an arithmetic average of the perpendicular and the parallel drag coefficient is assumed, the charge density becomes $\sim$10% less than that from Sträcke et al.'s (15) effective drag coefficient. In reality, microtubules were observed to tumble under the microscope.

The other governing property of the cantilever bending model is the flexural rigidity of microtubules. The dependency of this value on the length seems to be still in debate, but is attributed to the anisotropic microtubule structure associated with different lateral and longitudinal bonds of the protofilament-forming tubulin dimers. As evidence of the anisotropic structure of microtubules, Kis et al. experimentally found that the Young's modulus (E_{MT}) of microtubules is at least two orders of magnitude larger than the shear modulus (G_{MT}) by elastically deforming the lateral structure of microtubules with the tip of an atomic force microscope (32), and Pampaloni et al. reported that the ratio of E_{MT}/G_{MT} is as large as 10^6 (37). This observation is consistent with the interpretation that longitudinal interactions between α- and β-tubulin subunits (along protofilaments) are relatively stronger than the lateral interactions (circumferential direction). For isotropic and homogeneous material, we expect that the E_{MT} should be the same order of magnitude as the G_{MT} (44).

A question arises why microtubules are mechanically anisotropic. One highly feasible interpretation is that since longer microtubules can have more interactions/connections among the neighboring protofilaments than shorter ones, the more tightly bonded protofilaments exhibit reduced slipping between protofilaments and consequently bending, bringing about a mechanically stiffer structure (45,46). This explanation may also be supported by the fact that taxol-induced microtubules are more flexible than MAP (microtubule-associated-protein) stabilized microtubules (25,31,47), because taxol may weaken the interactions among the protofilaments, whereas MAPs are generally believed to strengthen them (45). This is further supported by VanBuren et al., who estimated that longitudinal bond energy between tubulin dimers is nearly two times stronger than lateral bond energy between tubulin dimers (34).

In addition, two related facts were revealed by recent numerical simulations by Kasas et al. (36) designed to verify the empirical results and analytical model suggested by Kis et al. (32). First, a significant difference in the estimated bending of microtubules could be produced by changing from a homogeneous model that assumed the same and constant modulus along (E_{MT} = 2 GPa) and between (G_{MT} = 2 GPa) the protofilaments, to the anisotropic model that assumed a different modulus along (E_{MT} = 2 GPa) and between (G_{MT} = 1.4 MPa) the protofilaments. Second, a 2 μm long microtubule that has 5% defects (missing tubulin subunits) showed $\sim$50% different deflection under a certain constant load (36). These two simulations further support the view that microtubules behave anisotropically. All of these reports are consistent with the observations and the modeling presented in this study. Finally, we suspect that microtubules can be locally buckled by externally applied forces, in which case, the cross section changes dramatically (e.g., ovalization), resulting in a severalfold reduction in the moment of inertia (48,49). Even though this ovalization mechanism cannot entirely explain the large disparity between the flexural rigidities that have been reported in the literature, it may contribute markedly to apparent differences in the flexural rigidity and larger deflections. As outlined in Appendix B, we suggest that ovalizations (locally) reduced the flexural rigidity of microtubules by $\sim$5-fold. Moreover, an apparently sharper bending at the interface of the bound and free portions of microtubules (for example, see Fig. 4 *b*) that could frequently be observed under the highest applied loads is also consistent with an ovalization of microtubules. Linear approximations based on results from the ovalization model (Appendix B) predict changes as large as 5–10° in the angular orientation of ovalized segments as short as 100 nm when microtubules are loaded under conditions resembling those used for experiments in this study. This will lead to clearly visible kinks adjacent to the clamped region that are distinct from the continuous bend of the cantilevered microtubule portion. Although this highlights the potential importance of ovalization for microtubule bending, other factors (including boundary conditions, microtubule discontinuities, and defects) might also contribute to remaining discrepancies between our observations and model predictions. Direct

experimental observations of the ovalization of microtubule should now be attempted to test this hypothesis.

In conclusion, we confirmed that microtubule gliding on kinesin-coated surfaces can be actively controlled to point microtubules toward any desired direction by (re)orienting their leading ends through the application of electric fields. Any mechanistic understanding or modeling of the bending mechanism of the leading ends under these applied fields requires detailed knowledge of the biophysical properties of microtubules, low Reynolds number hydrodynamics, and electrokinetics. These coupled mechanisms were investigated by carefully characterizing each of these properties. First, the charge density was determined by imposing an electrophoretic force on the negatively charged microtubules and quantifying the electrophoretic mobility of the microtubules. Second, the electroosmotic mobility of the buffer solution for gliding assays was measured by a caged dye method and a laser setup to find the viscous drag caused by electroosmotic flow. Last, the flexural rigidity was measured by using partly biotinylated microtubules that were immobilized via streptavidin linkages to BSA adsorbed to glass surfaces. This approach allowed us to carefully measure microtubule deflections under applied E-fields. To our surprise, but in agreement with recent reports from other groups, the flexural rigidity of microtubules depends on the microtubule length. On the basis of these measured biophysical properties of microtubules and by carefully considering the hydrodynamics and electrokinetics of kinesin-based microtubule transport assays, we were able to propose a nonlinear cantilever model that predicts the deflection and steering of microtubules by E-fields in gliding assays. Finally, we expect this model to further stimulate the development and provide quantitative insights into the engineering of kinesin- and microtubule-based transport systems for micro-/nanofluidic biotechnology applications.

APPENDIX A: EXACT ANALYTICAL SOLUTION OF AN ELASTIC CANTILEVER BEAM UNDER UNIFORM LOAD OR SELF-WEIGHT

According to the Bernoulli-Euler's curvature and bending moment theory, the radius of curvature (ρ) of a cantilever-beam subject to a uniform load (ω) is related to the bending moment as follows (43):

$$\frac{1}{\rho} = \frac{M}{EI} = \frac{d\psi}{ds}. \tag{A1}$$

Here, M is the bending moment, EI is flexural rigidity, s is the arc length, and ψ is the slope at s. In rectangular coordinates, $d\psi/ds$ is expressed as

$$\frac{d\psi}{ds} = \frac{d^2y/dx^2}{\left[1 + (dy/dx)^2\right]^{3/2}}. \tag{A2}$$

Typically, for a small deflection, this differential equation (Eq. A2) can be linearized by neglecting the geometrical nonlinearity created by $(dy/dx)^2$ term compared to unity. Assuming ideal boundary conditions ($y = 0$ and $dy/dx = 0$ at $x = 0$, clamped wall boundaries) and the bending moment ($M = -\omega(x - L)^2/2/EI$, the deflection is derived as follows:

$$\delta_{\text{linear}} = \frac{\omega L^4}{8EI}. \tag{A3}$$

However, for a large deflection, this linearized solution produces significant error. An exact solution of a cantilever beam subject to a uniformly distributed load is obtained by solving the governing equation for a bent elastic rod, as given in Frisch-Fray (43). The governing equation is

$$EI\frac{d^2\psi}{ds^2} - (T_0 - q_x s)\sin(\psi) + (S_0 + q_y s)\cos(\psi) = 0. \tag{A4}$$

As seen in Fig. 8, at an infinitesimal segment ds, the tension (T_0), the shear (S_0), and the uniform load in the x direction (q_x) at the origin of P are all zero. Since the only uniform load in the y direction (q_y) is ω (self-weight or vertical uniform load), and s is defined as the arc length from the free end indicated as S (refer to $x'y'$ coordinate), Eq. A4 becomes

$$EI\frac{d^2\psi}{ds^2} = -\omega s\cos(\psi). \tag{A5}$$

The boundary conditions are $d\psi/ds|_{s=0} = 0$ and $\psi(s = 0) = \psi_0$. From Eq. A5 and these boundary conditions, we have

$$\begin{aligned}
&\psi'(s = 0) = 0\\
&\psi''(s = 0) = 0\\
&\psi'''(s = 0) = -\frac{\omega}{EI}\cos(\psi_0)\\
&\psi^{(4)}(s = 0) = 0\\
&\psi^{(5)}(s = 0) = 0\\
&\psi^{(6)}(s = 0) = -2\left(\frac{\omega}{EI}\right)^2\sin(2\psi_0)\\
&\psi^{(7)}(s = 0) = 0\\
&\psi^{(8)}(s = 0) = 0\\
&\psi^{(9)}(s = 0) = \left(\frac{\omega}{EI}\right)^3\left[70\cos^3(\psi_0) - 14\sin(\psi_0)\sin(2\psi_0)\right]\\
&\psi^{(10)}(s = 0) = \ldots
\end{aligned} \tag{A6}$$

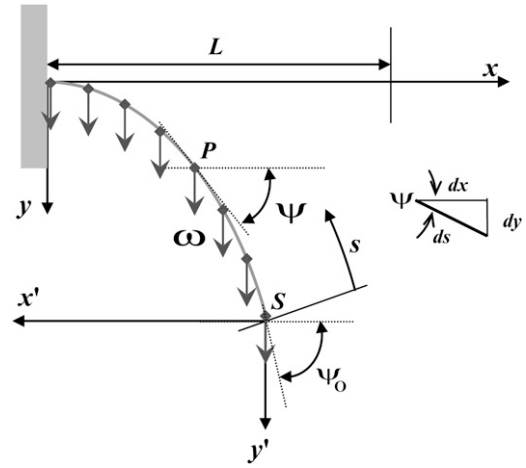

FIGURE 8 Elastic cantilever-beam under distributed loading. L is the total length of the cantilever, ω is a uniform load per unit length, ψ is the angle between the tangent at P and the x axis along the curvature of the cantilever, and s is the arc length from the free end (S).

By substituting these derivatives into a MacLaurin series, we get

$$\psi(s) = \psi_0 - \frac{\omega}{EI}\frac{\cos(\psi_0)}{6}s^3 - \left(\frac{\omega}{EI}\right)^2\frac{\sin(2\psi_0)}{360}s^6 + \left(\frac{\omega}{EI}\right)^3\left[\frac{\cos^3(\psi_0)}{5184} - \frac{\sin(\psi_0)\sin(2\psi_0)}{25920}\right]s^9 + \ldots \tag{A7}$$

Eq. A7 is rewritten as follows:

$$\psi(s) = \psi_0 + \beta$$

$$\text{where, } \beta = (a_3 s^3 + a_6 s^6 + a_9 s^9 + \ldots) = \sum_{k=1}^{\infty} a_{3k} s^{3k}. \tag{A8}$$

The coefficients of s are

$$a_3 = -\frac{\omega}{EI}\frac{\cos(\psi_0)}{6}$$

$$a_6 = -\left(\frac{\omega}{EI}\right)^2\frac{\sin(2\psi_0)}{360}$$

$$a_9 = \left(\frac{\omega}{EI}\right)^3\left[\frac{\cos^3(\psi_0)}{5184} - \frac{\sin(\psi_0)\sin(2\psi_0)}{25920}\right]. \tag{A9}$$

From the left boundary condition of $\psi(L) = 0$ at the clamped wall and Eq. A8, we get

$$0 = \psi_0 - \frac{\omega}{EI}\frac{\cos(\psi_0)}{6}L^3 - \left(\frac{\omega}{EI}\right)^2\frac{\sin(2\psi_0)}{360}L^6 + \left(\frac{\omega}{EI}\right)^3\left[\frac{\cos^3(\psi_0)}{5184} - \frac{\sin(\psi_0)\sin(2\psi_0)}{25920}\right]L^9. \tag{A10}$$

Hence, ψ_0 can be numerically obtained from Eq. A10. The vertical deflection and horizontal deflection are calculated by expanding $\sin(\beta)$ and $\cos(\beta)$, respectively, and then by integrating them as follows. The vertical deflection is

$$-y'(s) = \int_0^s \sin(\psi)ds = \int_0^s \sin(\psi_0)\cos(\beta) + \cos(\psi_0)\sin(\beta)ds = \sin(\psi_0)s - \frac{\omega}{EI}\frac{\cos^2(\psi_0)}{24}s^4 - \left(\frac{\omega}{EI}\right)^2\frac{\sin(\psi_0)\cos^2(\psi_0)}{360}s^7 - \left(\frac{\omega}{EI}\right)^3\left[\frac{\cos^4(\psi_0)}{10368} - \frac{13\sin^2(\psi_0)\cos^2(\psi_0)}{129600}\right]s^{10} + \ldots \tag{A11}$$

The horizontal deflection is

$$x'(s) = \int_0^s \cos(\psi)ds = \int_0^s \cos(\psi_0)\cos(\beta) - \sin(\psi_0)\sin(\beta)ds = \cos(\psi_0)s + \frac{\omega}{EI}\frac{\sin(2\psi_0)}{48}s^4 + \left(\frac{\omega}{EI}\right)^2\frac{\sin(\psi_0)\sin(2\psi_0)}{2520}s^7 - \left(\frac{\omega}{EI}\right)^2\frac{\cos^3(\psi_0)}{504}s^7 - \left(\frac{\omega}{EI}\right)^3\frac{49\sin(\psi_0)\cos^3(\psi_0)}{259200}s^{10} + \left(\frac{\omega}{EI}\right)^3\frac{\sin^3(\psi_0)\cos(\psi_0)}{129600}s^{10} + \ldots. \tag{A12}$$

If $s = L$ and ψ_0 is small, Eq. A10 gives rise to ψ_0, which agrees with the elementary theory

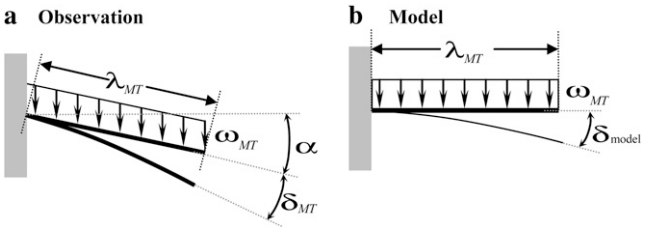

FIGURE 9 Microtubule and E-field orientation. (*a*) Illustration of a randomly oriented (with respect to the E-field) cantilever beam subject to a uniform load (analogous to cantilevered microtubules in the presence of an E-field) and (*b*) a cantilever beam that is oriented perfectly perpendicular to the load direction.

$$\psi_0 = \frac{\omega L^3}{6EI}. \tag{A13}$$

By substituting s with L in Eq. A11, we can obtain the exact analytical maximum deflection of a cantilever beam:

$$\delta_{\text{nonlinear}} = \sin(\psi_0)L - \frac{\omega}{EI}\frac{\cos^2(\psi_0)}{24}L^4 - \left(\frac{\omega}{EI}\right)^2\frac{\sin(\psi_0)\cos^2(\psi_0)}{360}L^7 - \left(\frac{\omega}{EI}\right)^3\left[\frac{\cos^4(\psi_0)}{10368} - \frac{13\sin^2(\psi_0)\cos^2(\psi_0)}{129600}\right]L^{10} + \ldots. \tag{A14}$$

In case of a small deflection, the $\delta_{\text{nonlinear}}$ becomes identical with the elementary theory of Eq. A3 (δ_{linear}).From Eq. A3, the deflection (δ_{MT}) of Fig. 9 *a*, which is analogous to the experimentally observed deflection, is related with δ_{model} of Fig. 9 *b*, which is analogous to our model as follows:

$$\delta_{\text{model}} = \frac{\delta_{\text{MT}}}{\cos(\alpha)}. \tag{A15}$$

This relationship was used in linearly compensating for the observed deflections for a convenient comparison to the model, because most of the observed deflections have their own individual incident angles to the E-field relative to the microtubule cantilever.

APPENDIX B: OVALIZATION MODEL OF MICROTUBULES

We hypothesize that ovalization and local buckling of microtubules can significantly affect the moment of inertia of the microtubule cross section (Fig. 10), especially under larger loads. That is, when a microtubule is subject to a bending moment exerted by an electrophoretic force or a viscous drag force, the tensile and compressive longitudinal stresses on opposite sides of the natural plane might deform the cross section of the original microtubule tube into an oval shape. This bending moment-induced ovalization instability for shells (which can be easily observed when applying a bending moment to a drinking straw) was investigated by Calladine (49) and Brazier (48). From known mechanical properties of microtubules (except Poisson's ratio), the critical bending moment at which ovalization takes place can be described as (48)

$$M_{\text{crit}} = \frac{2\sqrt{2}}{9}\frac{\pi E_{\text{MT}}}{\sqrt{1-\upsilon^2}}r_{\text{m}}t^2. \tag{B1}$$

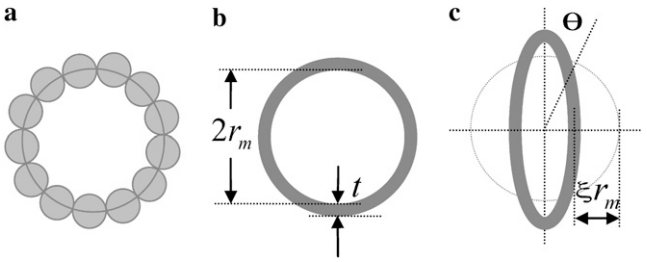

FIGURE 10 Effect of ovalization. (*a*) An illustration of the cross section of a microtubule consisting of 13 protofilaments. (*b*) A tube that models the cross section of the microtubule with a uniform thickness (t). (*c*) Cross section of a microtubule subjected to a bending moment that leads to ovalization and buckling.

Here, E_{MT} is the Young's modulus, υ is the Poisson's ratio, r_m is the mean radius of the microtubule, and t is the wall thickness of the microtubule. Poisson's ratio for microtubules has not yet been measured, but was assumed to be 0.3, which is a nominal value for homogeneous isotropic materials, close to that of other macromolecules (44). Measured Young's moduli for microtubules have large uncertainties and are found to fall into the range from 0.1 to 1.4 GPa (28–30,32,44). The mean radius of microtubules, r_m, is 12.83 nm, consistent with a wall thickness (t) of 2.7 nm and an inner radius (r_i) of microtubules of 11.48 nm (50).

From Eq. B1, the critical bending moment can be calculated to be ~10 pN·μm by assuming that $E_{MT} = 0.1$ GPa (32), which is on the same order of the moment imposed on a 10 μm-long microtubule by a 50 V/cm E-field (about 3 pN·μm). However, if local buckling occurs in response to thermal fluctuations, ovalization may take place more readily. By way of analogy, a typical empty aluminum soda can easily supports the weight of a human, but immediately fails if one dimples the sides of the can. By adopting the model of Brazier (48), the radial component of displacement (Ω) and circumferential component of displacement (Θ) are approximately

$$\Omega = r_m \xi \cos(2\theta) \tag{B2}$$

$$\Theta = -\frac{1}{2} r_m \xi \sin(2\theta). \tag{B3}$$

With the assumption of an ovalization amplitude ($\xi = 0.8$) (typically, local buckling occurs approximately at $\xi = 0.14$) (51), the moment of inertia of the oval cross section of the microtubule can be calculated as

$$I(\xi) = \int_{r_m - t/2}^{r_m + t/2} \int_0^{2\pi} [(\omega + r_m)\sin(\theta) + v\cos(\theta)]^2 r dr d\theta. \tag{B4}$$

The ovalization model predicts reductions of the original moment of inertia of up to a factor of 5 ($I(\xi = 0.8)/I(\xi = 0) = 1/5$). Fig. 10 illustrates the modeled microtubule and ovalization mechanism. Thus, ovalization could readily explain the slight difference between the cantilever model and observed deflection data. From the above model, we can also predict how a microtubule would deflect in our E-field-based flexural rigidity test if indeed an ovalization of the cantilevered portion would develop adjacent to the clamped portion. Assuming that the original moment of inertia declines by up to fivefold due to ovalization in a highly localized region that is only a few microtubule diameters in length (say 100 nm), the largest angular changes in the orientation of the ovalized region are expected to reach 10° when microtubules experience loads, as in some experiments in this study, that cause maximum deflections of ~20% of the cantilever length. Such large angular changes of a short, ovalized microtubule section should appear as sharp bends or kinks relative to the gentle bend of the deflected microtubule. Our microscopy data (for example, Fig. 4) support the existence of such ovalized microtubule sections; but other mechanisms, such as defects or discontinuities in the microtubule, could also account for the observed microtubule shapes.

This work was supported by National Science Foundation (BES 0428090) and Defense Advanced Research Projects Agency (N66001-02-C-8039) grants to E.M. and E.F.H.

REFERENCES

1. Howard, J. 2001. Mechanics of Motor Proteins and the Cytoskeleton. Sinauer Associates, Sunderland, MA.
2. Schliwa, M. 2003. Molecular Motors. Wiley-VCH, Weinheim, Germany.
3. Jia, L., S. G. Moorjani, T. N. Jackson, and W. O. Hancock. 2004. Microscale transport and sorting by kinesin molecular motors. *Biomed. Microdevices*. 6:67–74.
4. Bull, J. L., A. J. Hunt, and E. Meyhöfer. 2005. A theoretical model of a molecular-motor-powered pump. *Biomed. Microdevices*. 7:21–33.
5. Hess, H., G. D. Bachand, and V. Vogel. 2004. Powering nanodevices with biomolecular motors. *Chemistry (Easton)*. 10:2110–2116.
6. Hiratsuka, Y., T. Tada, K. Oiwa, T. Kanayama, and T. Q. Uyeda. 2001. Controlling the direction of kinesin-driven microtubule movements along microlithographic tracks. *Biophys. J*. 81:1555–1561.
7. Clemmens, J., H. Hess, J. Howard, and V. Vogel. 2003. Analysis of microtubule guidance in open microfabricated channels coated with the motor protein kinesin. *Langmuir*. 19:1738–1744.
8. Cheng, L. J., M. T. Kao, E. Meyhöfer, and L. J. Guo. 2005. Highly efficient guiding of microtubule transport with imprinted CYTOP nanotracks. *Small*. 1:409–414.
9. Dennis, J. R., J. Howard, and V. Vogel. 1999. Molecular shuttles: directed motion of microtubules slang nanoscale kinesin tracks. *Nanotechnology*. 10:232–236.
10. Clemmens, J., H. Hess, R. Lipscomb, Y. Hanein, K. F. Bohringer, C. M. Matzke, G. D. Bachand, B. C. Bunker, and V. Vogel. 2003. Mechanisms of microtubule guiding on microfabricated kinesin-coated surfaces: chemical and topographic surface patterns. *Langmuir*. 19: 10967–10974.
11. Lin, C. T., M. T. Kao, K. Kurabayashi, and E. Meyhöfer. 2006. Efficient designs for powering microscale devices with nanoscale biomolecular motors. *Small*. 2:281–287.
12. Kim, T., M.-T. Kao, E. Meyhöfer, and E. F. Hasselbrink. 2007. Biomolecular motor-driven microtubule translocation in the presence of shear flow: analysis of redirection behaviours. *Nanotechnology*. 18:025101–025109.
13. Sträcke, R., K. J. Bohm, J. Burgold, H. J. Schacht, and E. Unger. 2000. Physical and technical parameters determining the functioning of a kinesin-based cell-free motor system. *Nanotechnology*. 11:52–56.
14. Yokokawa, R., S. Takeuchi, T. Kon, M. Nishiura, K. Sutoh, and H. Fujita. 2004. Unidirectional transport of kinesin-coated beads on microtubules oriented in a microfluidic device. *Nano Lett*. 4:2265–2270.
15. Sträcke, R., K. J. Bohm, L. Wollweber, J. A. Tuszynski, and E. Unger. 2002. Analysis of the migration behaviour of single microtubules in electric fields. *Biochem. Biophys. Res. Commun*. 293:602–609.
16. van den Heuvel, M. G., M. P. de Graaff, and C. Dekker. 2006. Molecular sorting by electrical steering of microtubules in kinesin-coated channels. *Science*. 312:910–914.
17. Riveline, D., A. Ott, F. Julicher, D. A. Winkelmann, O. Cardoso, J. J. Lacapere, S. Magnusdottir, J. L. Viovy, L. Gorre-Talini, and J. Prost. 1998. Acting on actin: the electric motility assay. *Eur. Biophys. J*. 27: 403–408.
18. Kim, T., M. T. Kao, E. F. Hasselbrink, and E. Meyhöfer. 2007. Active alignment of microtubules with electric fields. *Nano Lett*. 7:211–217.
19. Kirby, B. J., and E. F. Hasselbrink Jr. 2004. Zeta potential of microfluidic substrates: 1. Theory, experimental techniques, and effects on separations. *Electrophoresis*. 25:187–202.
20. Hunt, A. J., F. Gittes, and J. Howard. 1994. The force exerted by a single kinesin molecule against a viscous load. *Biophys. J*. 67:766–781.
21. Nogales, E., S. G. Wolf, and K. H. Downing. 1998. Structure of the alpha beta tubulin dimer by electron crystallography. *Nature*. 391:199–203.

22. Minoura, I., and E. Muto. 2006. Dielectric measurement of individual microtubules using the electroorientation method. *Biophys. J.* 90:3739–3748.

23. van Mameren, J. 2002. Single molecule mechanics of biopolymers: an optical tweezers study. Master's thesis. Vrije Universiteit, Amsterdam.

24. Janson, M. E., and M. Dogterom. 2004. A bending mode analysis for growing microtubules: evidence for a velocity-dependent rigidity. *Biophys. J.* 87:2723–2736.

25. Felgner, H., R. Frank, and M. Schliwa. 1996. Flexural rigidity of microtubules measured with the use of optical tweezers. *J. Cell Sci.* 109:509–516.

26. Allersma, M. W. 2000. Motor protein and microtubule mechanics: application of a novel high-resolution optical trapping technique. PhD thesis. University of Michigan, Ann Arbor, MI.

27. Kikumoto, M., M. Kurachi, V. Tosa, and H. Tashiro. 2006. Flexural rigidity of individual microtubules measured by a buckling force with optical traps. *Biophys. J.* 90:1687–1696.

28. Venier, P., A. C. Maggs, M. F. Carlier, and D. Pantaloni. 1994. Analysis of microtubule rigidity using hydrodynamic flow and thermal fluctuations. *J. Biol. Chem.* 269:13353–13360.

29. Gittes, F., B. Mickey, J. Nettleton, and J. Howard. 1993. Flexural rigidity of microtubules and actin filaments measured from thermal fluctuations in shape. *J. Cell Biol.* 120:923–934.

30. Mickey, B., and J. Howard. 1995. Rigidity of microtubules is increased by stabilizing agents. *J. Cell Biol.* 130:909–917.

31. Kurachi, M., M. Hoshi, and H. Tashiro. 1995. Buckling of a single microtubule by optical trapping forces: direct measurement of microtubule rigidity. *Cell Motil. Cytoskeleton.* 30:221–228.

32. Kis, A., S. Kasas, B. Babic, A. J. Kulik, W. Benoit, G. A. Briggs, C. Schonenberger, S. Catsicas, and L. Forro. 2002. Nanomechanics of microtubules. *Phys. Rev. Lett.* 89:248101.

33. Takasone, T., S. Juodkazis, Y. Kawagishi, A. Yamaguchi, S. Matsuo, H. Sakakibara, H. Nakayama, and H. Misawa. 2002. Flexural rigidity of a single microtubule. *Jpn. J. Appl. Phys.* 41:3015–3019.

34. VanBuren, V., D. J. Odde, and L. Cassimeris. 2002. Estimates of lateral and longitudinal bond energies within the microtubule lattice. *Proc. Natl. Acad. Sci. USA.* 99:6035–6040.

35. Kasas, S., C. Cibert, A. Kis, P. De Los Rios, B. M. Riederer, L. Forro, G. Dietler, and S. Catsicas. 2004. Oscillation modes of microtubules. *Biol. Cell.* 96:697–700.

36. Kasas, S., A. Kis, B. M. Riederer, L. Forro, G. Dietler, and S. Catsicas. 2004. Mechanical properties of microtubules explored using the finite elements method. *ChemPhysChem.* 5:252–257.

37. Pampaloni, F., G. Lattanzi, A. Jonas, T. Surrey, E. Frey, and E. L. Florin. 2006. Thermal fluctuations of grafted microtubules provide evidence of a length-dependent persistence length. *Proc. Natl. Acad. Sci. USA.* 103:10248–10253.

38. Lakamper, S., A. Kallipolitou, G. Woehlke, M. Schliwa, and E. Meyhöfer. 2003. Single fungal kinesin motor molecules move processively along microtubules. *Biophys. J.* 84:1833–1843.

39. Paul, P. H., M. G. Garguilo, and D. J. Rakestraw. 1998. Imaging of pressure- and electrokinetically driven flows through open capillaries. *Anal. Chem.* 70:2459–2467.

40. Devasenathipathy, S., J. G. Santiago, S. T. Wereley, C. D. Meinhart, and K. Takehara. 2003. Particle imaging techniques for microfabricated fluidic systems. *Exp. Fluids.* 34:504–514.

41. Probstein, R. F. 2003. Physicochemical Hydrodynamics: An Introduction. 2nd ed. John Wiley & Sons, New York.

42. Xuan, X. C., D. Sinton, and D. Q. Li. 2004. Thermal end effects on electroosmotic flow in a capillary. *Int. J. Heat Mass Tran.* 47:3145–3157.

43. Frisch-Fay, R. 1962. Flexible Bars. Butterworths, London.

44. Tuszynski, J. A., T. Luchko, S. Portet, and J. M. Dixon. 2005. Anisotropic elastic properties of microtubules. *Eur. Phys. J. E.* 17:29–35.

45. Dye, R. B., S. P. Fink, and R. C. Williams. 1993. Taxol-induced flexibility of microtubules and its reversal by Map-2 and Tau. *J. Biol. Chem.* 268:6847–6850.

46. Sept, D., N. A. Baker, and J. A. McCammon. 2003. The physical basis of microtubule structure and stability. *Protein Sci.* 12:2257–2261.

47. Kurz, J. C., and R. C. Williams. 1995. Microtubule-associated proteins and the flexibility of microtubules. *Biochemistry.* 34:13374–13380.

48. Brazier, L. G. 1927. On the flexure of thin cylindrical shells and other ''thin'' sections. *Proc. Royal Society of London Series A—Containing Papers of a Mathematical and Physical Character*. 116:104–114.

49. Calladine, C. R. 1983. Theory of Shell Structures. Cambridge University Press, New York.

50. Mickey, B., F. Gittes, and J. Howard. 1993. Taxol increases the flexural rigidity of microtubules. *Biophys. J.* 64:A261. (Abstr.)

51. Vodenitcharova, T., and L. C. Zhang. 2003. Effective wall thickness of a single-walled carbon nanotube. *Phys. Rev. B.* 68:165401–165404.

52. Gittes, F., E. Meyhöfer, S. Baek, and J. Howard. 1996. Directional loading of the kinesin motor molecule as it buckles a microtubule. *Biophys. J.* 70:418–429.

53. Hunt, A. J., and J. Howard. 1993. Kinesin swivels to permit microtubule movement in any direction. *Proc. Natl. Acad. Sci. USA.* 90:11653–11657.